

Theoretical Solutions for Dynamic Characteristics of Spiral-Grooved Liquid Seals

Lulu Zhai, Zuchao Zhu, Zhenjie Zhang, Jia Guo & Baoling Cui

To cite this article: Lulu Zhai, Zuchao Zhu, Zhenjie Zhang, Jia Guo & Baoling Cui (2018): Theoretical Solutions for Dynamic Characteristics of Spiral-Grooved Liquid Seals, Tribology Transactions, DOI: [10.1080/10402004.2018.1463427](https://doi.org/10.1080/10402004.2018.1463427)

To link to this article: <https://doi.org/10.1080/10402004.2018.1463427>



Accepted author version posted online: 23 Apr 2018.
Published online: 09 Nov 2018.



[Submit your article to this journal](#)



Article views: 50



[View Crossmark data](#)



Citing articles: 1 [View citing articles](#)



Theoretical Solutions for Dynamic Characteristics of Spiral-Grooved Liquid Seals

Lulu Zhai^a, Zuchao Zhu^a, Zhenjie Zhang^a, Jia Guo^b, and Baoling Cui^a

^aKey Laboratory of Fluid Transmission Technology of Zhejiang Province, Zhejiang Sci-Tech University, Hangzhou, P. R. China; ^bZhejiang Institute of Mechanical & Electrical Engineering Co., Ltd, Hangzhou, P. R. China

ABSTRACT

Annular seals represent one of the solutions for controlling leakage in high-speed turbomachinery, especially in multistage centrifugal pumps. In this article, a theoretical analysis method for leakage rate and dynamic characteristics of spiral-grooved liquid seals based on the theory of Iwatsubo and Childs is proposed. Steady-state velocities and leakage rate are figured out first with the inertia term of the fluid within the seals. Subsequently, governing equations for the land part and the groove part including the axial momentum equation, circumferential momentum equation, and continuity equation are respectively built. A solution method for calculating the rotordynamic characteristics that has taken account of the circumferential velocity perturbation change with the axial location is developed by solving the first-order governing equations. Detailed comparisons between the experimental leakage rates and theoretical predictions show good agreement. Moreover, dynamic coefficients predicted by the proposed method are compared with the theoretical and experimental results of Iwatsubo. The results show that the predicted stiffness of the present solution method correlates well with the experimental evidence with an error of less than 35% in the given examples, which validates the analysis method developed in this article. The predicted accuracy of stiffness and damping coefficients has improved substantially compared to the accuracy of the solution method proposed by Iwatsubo.

ARTICLE HISTORY

Received 18 September 2017
Accepted 6 April 2018

KEYWORDS

Spiral-grooved liquid seal;
dynamic characteristics;
perturbation method

Introduction

Annular liquid seals are primarily used to control the leakage in turbomachinery, especially in multistage centrifugal pumps such as boiler feed pumps and other heavy-duty pumps. The leakage flow within the seals not only contributes to an increase of loss generation, but also induces fluid forces, which has significant effects on the rotordynamic characteristics of the pump. In order to investigate the physics of the leakage flow and its influence on the rotordynamic behavior of the whole pump, the fluid-induced force is simplified as a series of rotordynamic characteristics of annular seals based on a linear kinetic model. With the improvement of hydraulic performances of pumps, liquid annular seals that will facilitate superior rotordynamic characteristics while providing good leakage control are in great need. Due to the inward pumping actions, spiral-grooved liquid seals will minimize the leakage rate, as well as generating load capacity and stiffness, which will contribute a lot to the improvements in hydraulic performance and pump reliability. Therefore, these seals are gradually being used in heavy-duty pumps for coal chemical and petrochemical industries.

For decades, researchers and engineers have done lots of work on the sealing and dynamic characteristics of annular seals with spiral grooves or other kinds of grooves based on

the bulk-flow model, which does not consider the fluctuations in local velocities due to turbulence or the shape of the velocity profiles but only relate average fluid velocity to wall shear stresses. Vohr and Chow applied the Elrod–Ng–Pan turbulence theory to the dynamic analysis of spiral-grooved journal bearing (1) and the static analysis of spiral-grooved seals (2) operated in a turbulent regime. Zuk (3) analyzed the static characteristics of the spiral-grooved seal by solving the Navier–Stokes equation with a finite difference method. Iwatsubo (4–6) refined Kostyuk’s model for gas labyrinth seals by introducing the time dependency of area change and theoretically analyzed the static and dynamic characteristics of parallel-grooved, spiral-grooved, and double spiral-grooved seals based on those for spiral-grooved bearings. However, in these theoretical analyses, the fluid governing equations included only the axial momentum equation and the continuity equation, but ignored the circumferential momentum equation and the changes of circumferential velocity perturbation with the axial location, which is not adequate for liquid annular seals because of the high axial and circumferential Reynolds numbers. Nordmann et al. (7) and Kim (8) studied the leakage and dynamic characteristics of parallel-grooved and spiral-grooved seals by introducing equivalent roughness coefficients in both the circumferential and axial directions based

Nomenclature

C	= direct damping
C_{10}	= mean clearance of the seal
c	= cross-coupled damping
H	= clearance function
I_s	= thread number
K	= direct stiffness
k	= cross-coupled stiffness
L	= length of the spiral-grooved seal
l_l	= land width in the ζ -direction
L_g	= groove width in the ζ -direction
N	= number of stages
$P, \Delta P$	= pressure difference
Pe	= effective pressure difference
T	= groove depth
R	= seal radius
Re_{qu}	= equivalent radius
Re_{θ}	= circumferential Reynolds number
u	= fluid velocity
t	= time
x	= x -direction
y	= y -direction
α	= spiral angle

γ	= divergent flow angle
ε	= eccentricity ratio, induced as the perturbation coefficient
λ	= friction coefficient
μ	= dynamic viscosity
τ	= shear stress
ν	= kinematic viscosity
ζ	= pressure loss coefficient
ρ	= fluid density
Ω	= whirling velocity
ω	= rotating speed

Subscripts

0	= zeroth-order perturbation solutions
1	= first-order perturbation solutions
g	= groove portion
l	= land portion
s	= spiral-grooved seal
z	= z -direction
ζ	= ζ -direction
η	= η -direction
θ	= θ -direction
in	= inlet pressure loss
out	= outlet pressure loss

on Hirs's turbulent lubrication theory and "fine groove" theory. Florjancic (9) and Marquette (10) developed a three-control-volume approach for liquid circumferentially grooved seals, featuring an excellent description of the flow inside the groove cavity. Nagai (11) introduced an oblique coordinate system to the static analysis of a spiral-grooved seal, in which the governing equations included the effects of fluid inertia and energy loss during the passage between the groove and land parts. A series of experiments for leakage flow rates was conducted to verify the proposed method. Additionally, Pape and Vrakking (12), Ketola and McGrew (13), and Stair and Hale (14) gave the sealing performance of spiral-grooved seals in turbulent regime by an experimental method. Kanki and Kawakami (15) and Iwatsubo et al. (16) experimentally investigated the leakage characteristics, load capacity, and dynamic characteristics for spiral-grooved seals with helical angle less than 20 degrees. Childs and Nolan (17,18) tested the leakage rate and dynamic characteristics of 7 sets of spiral-grooved seals whose helical angle varied from 0 to 70 degrees. Childs (19) tested the leakage and rotordynamic characteristics of three grooved seals with helix angles of 0°, 15, and 30° against rotation, and compared the characteristics of honeycomb seals of the same size. Proctor and Delgado (20) tested a noncontacting finger seal operating adjacent to a herringbone-grooved rotor under various operating conditions.

With the development of computational fluid dynamics (CFD), the sealing and dynamic characteristics of annular seals with complex geometries have been investigated using CFD-based methods. In this method, the fundamental Navier–Stokes equations for fluid flow within the seal clearances can be solved by dividing an arbitrarily shaped volume of fluid into a discrete number of nodes at which unknown variables like velocity, pressure, and all the details of the flow field can be solved in theory, which makes the dynamic prediction more accurate. Bhattacharya (21), Nielsen (22),

Kirk and Gao (23–25), and Untaroiu (26,27) made further implementation and validation for the steady-state whirling rotor model for the predictions of dynamic forces and leakage rate of seals with different grooves including stepped grooves and circumferential grooves. Chochua and Soulas (28), Yan et al. (29), and Nielsen et al. (30) investigated the hole-pattern seal and convergent honeycomb seal using the CFD-based Instationary Perturbation Model (IPM) and compared the results with the results of experiments and ISOTSEAL bulk-flow code. Sivakumar et al. (31) developed a computational framework based on combined three-dimensional (3D) finite-element (FE)/CFD methodology and numerically investigated the influence of centrifugal growth on the rotor dynamic characteristics of a typical rotating straight-groove gas seal.

The improved prediction capabilities of CFD method come at much higher computational costs. Therefore, CFD-based methods are mainly used only in the research field, while theoretical prediction procedures based on the bulk-flow model are still the main method for calculating leakage rate and dynamic characteristics in engineering. Extensive theoretical analysis for leakage flow rate and dynamic characteristics of spiral-grooved seals is still needed.

In this article, a systematic solution method for dynamic characteristics of spiral-grooved liquid seals (SGLSs) is proposed based on bulk-flow model. The present analysis of the performance of SGLSs combines the prior steady flow characteristics analysis performed by Iwatsubo (5) with the solution method for governing equations formulated by Childs (32). It is noted that in the present method, the circumferential momentum equation and circumferential velocity perturbation terms that are neglected in Iwatsubo's solution method will be retained. The steady-state velocities and pressures and the leakage rates considering pumping actions of the spiral grooves are solved first based on the solutions proposed by Iwatsubo. Then a solution method for governing equations including the axial

momentum equation, circumferential momentum equation, and continuity equation, as well as dynamic characteristics, is developed similar to the finite-length solution method proposed by Childs. Moreover, detailed comparisons are conducted between theoretical and experimental leakage rates, rotordynamic characteristics, and hydraulic forces coefficients conducted by Iwatsubo to validate the proposed solution method.

Theoretical analysis

Modeling

In this article, a smooth-stator/spiral-grooved-rotor seal is selected as the research model and the spiral angle is less than 15 degrees. Figure 1 shows a spiral-grooved rotor. As shown, there are two kinds of parts within the grooved rotors: the land parts and the spiral groove parts, which play an active role in restricting leakage flow from the high-pressure side to the lower pressure side. The enlarged radial clearances between the rotor and the stator, combined with large pressure differences and low viscosity liquids, make the flow in the clearance paths highly turbulent. Hence, the Reynolds equations that have been used for bearings and viscoseals are not adequate (33).

Referring to Iwatsubo's analysis (5), a η - ζ coordinate system is built as shown in Figs. 2a and 2b to analyze the static characteristics of the spiral-grooved part. The η -direction and ζ -direction are respectively set parallel and perpendicular to the groove direction. Flow between the groove land and the stator along the η -direction is approximated as a flow between two parallel plates, and the flow in the groove is approximated as the flow in a rectangular-cross-sectional tube. The vortex in the ζ -direction of the spiral-grooved seal is supposed to diverge with the angle γ and then go to the next land, as shown in Fig. 2c.

Leakage flow rate of spiral-grooved seals

Pumping flow within spiral-grooved seals is the result of the component of rotational velocity of spiral-grooved rotor along the groove direction. This flow will increase the resistance to the axial flow, while retarding the development of circumferential flow in the direction of shaft rotation, which is known as the "pumping effect" of spiral-grooved seals.

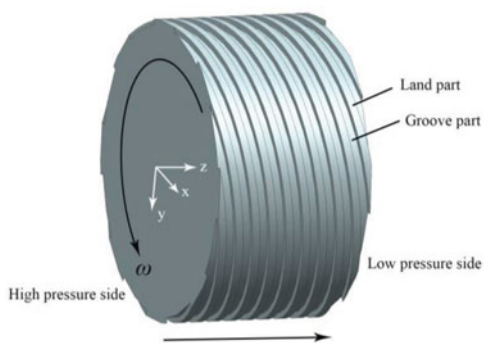
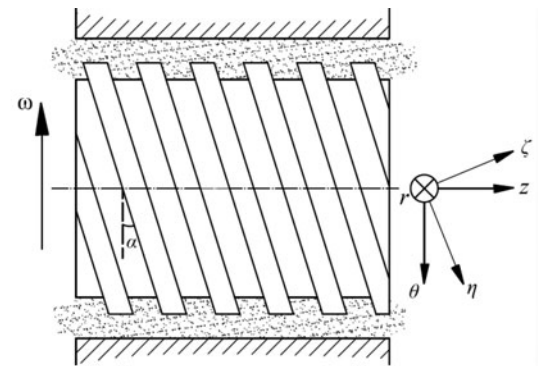
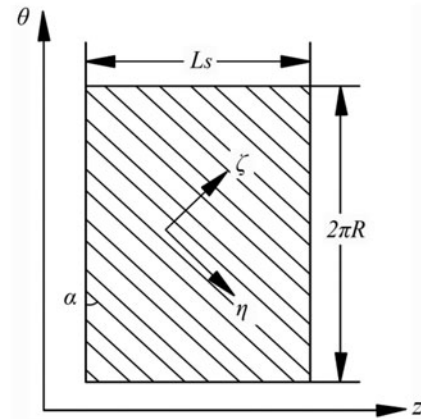


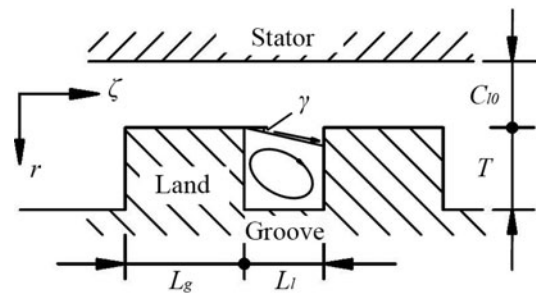
Figure 1. 3D model of a spiral-grooved rotor.



(a)



(b)



(c)

Figure 2. (a) Front view of the spiral-grooved rotor. (b) Expanded top-view figure of the spiral-grooved rotor. (c) Cross-sectional view of the spiral-grooved part.

Effective pressure difference across the spiral-grooved part is the result of operating pressure and the pumping effects induced by spiral grooves. The pressure difference generated by the pumping effect is described based on the experimental results of Vohr and Chow (2). The equivalent pressure difference due to the pumping action is shown as Eq. [A.1] provided in Appendix A and is thoroughly discussed in Vohr and Chow (2) and Iwatsubo et al. (5).

Fluid flows within the land part and the groove part are analyzed separately. Besides, the fluid velocities within each part in η - and ζ -directions are derived separately according to a pressure equilibrium between the effective pressure difference and pressure losses due to wall friction, the inlet and outlet contraction effect. The pressure equilibrium relations

in the η -direction and in the ζ -direction within the land region are provided as Eq. [A.2] and Eq. [A.3] of [Appendix A](#).

Similar to the analytical method for straight labyrinth seals proposed by Iwatusbo (4), the total pressure drop across the spiral-grooved part in the ζ -direction is the sum of pressure losses of each stage as stated in Eq. [1]:

$$\begin{aligned}
P - \Delta P_{\text{pumping}} &= (N - 1) \cdot (\Delta P_{l\zeta\lambda} + \Delta P_{l\zeta\text{out}'} + \Delta P_{g\zeta\lambda} + \Delta P_{l\zeta\text{in}'} \\
&\quad + \Delta P_{l\zeta\lambda} + \Delta P_{l\zeta\text{in}} + \Delta P_{l\zeta\text{out}} \\
&= (N - 1) \cdot \left[\frac{1}{2} \rho \lambda_{l\zeta} u_{l\zeta 0}^2 \frac{2L_l}{C_{l0}} + \frac{1}{2} \rho (1 - \xi_{l\zeta\text{out}'}) u_{l\zeta 0}^2 \right. \\
&\quad + \frac{1}{2} \rho \lambda_{g\zeta} u_{l\zeta 0}^2 \frac{L_g}{2C_{l0}} + \frac{1}{2} \rho (1 + \xi_{l\zeta\text{in}'}) u_{l\zeta 0}^2 \left. \right] \\
&\quad + \frac{1}{2} \rho \lambda_{l\zeta} u_{l\zeta 0}^2 \frac{2L_l}{C_{l0}} + \frac{1}{2} \rho (1 + \xi_{l\zeta\text{in}}) u_{l\zeta 0}^2 \\
&\quad + \frac{1}{2} \rho (1 - \xi_{l\zeta\text{out}}) u_{l\zeta 0}^2
\end{aligned} \tag{1}$$

Fluid velocities $u_{\eta 0}$, $u_{g\eta 0}$, and $u_{l\zeta 0}$ can be figured out by solving Eq. [A.2], Eq. [A.3], and Eq. [1], respectively. The friction factors λ_{η} , $\lambda_{g\eta}$, $\lambda_{l\zeta}$, and $\lambda_{g\zeta}$ are determined by Hirs's turbulent lubrication equations developed in 1974 (34). The inlet and outlet pressure loss coefficients $\xi_{\eta\text{in}}$, $\xi_{\eta\text{out}}$, $\xi_{g\eta\text{in}}$, $\xi_{g\eta\text{out}}$, $\xi_{l\zeta\text{in}}$, $\xi_{l\zeta\text{out}}$, $\xi_{l\zeta\text{in}'}$, $\xi_{l\zeta\text{out}'}$ are determined referring to Iwatusbo's theoretical approach for spiral-grooved seals in Iwatusbo et al. (4) and Iwatusbo et al. (5). Therefore, the steady flow velocities in the axial and circumferential directions $u_{\theta 0}$, $u_{z 0}$, $u_{\theta g 0}$, and $u_{z g 0}$ and total leakage flow rate Q can be obtained by Iwatusbo's equations shown in [Appendix A](#).

Rotordynamic characteristics of SGLSs

Governing equations

In the present research, the "fine groove" assumption is used to account for grooving patterns on the spiral-grooved seal surface. Under the assumption, only the average variables across a land and a groove at every point along the seal length direction should be solved to calculate the dynamic characteristics of spiral-grooved seals, while the actual sawtooth profile of pressure and the actual variation of velocities along the seal length are not required. The wall shear stresses, velocities, and pressure for grooved seals in the analysis follow this averaging concept coupled with the bulk-flow model. Governing equations including the continuity equation, circumferential momentum equation, and axial momentum equation are built, and the shear stresses are discussed in detail in Iwatusbo et al. (5). The equations and stresses are listed in [Appendix A](#).

The present analysis for dynamic characteristics of spiral-grooved seals is begun by substituting $\tau_{z\lambda}$, τ_{zg} , $\tau_{\theta\lambda}$, and $\tau_{\theta g}$ (listed from Eq. [A.9] to Eq. [A.12]) into the governing equations (demonstrated as Eq. [A.6] to Eq. [A.8]). Thus, governing equations for the land and the groove part are respectively obtained in the following.

For the land part:

$$\frac{\partial H}{\partial t} + \frac{\partial(Hu_{\theta l})}{R\partial\theta} + \frac{\partial(Hu_{z l})}{\partial z} = 0 \tag{2}$$

$$\rho H \left(\frac{\partial u_{\theta l}}{\partial t} + u_{\theta l} \frac{\partial u_{\theta l}}{R\partial\theta} + u_{z l} \frac{\partial u_{\theta l}}{\partial z} \right) = -H \frac{\partial P_l}{R\partial\theta} - \rho \lambda_{z l} u_{z l} \left(u_{\theta l} - \frac{1}{2} R\omega \right) \tag{3}$$

$$\rho H \left(\frac{\partial u_{z l}}{\partial t} + u_{\theta l} \frac{\partial u_{z l}}{R\partial\theta} + u_{z l} \frac{\partial u_{z l}}{\partial z} \right) = -H \frac{\partial P_l}{\partial z} - \rho \lambda_{z l} u_{z l}^2 \tag{4}$$

For the groove part:

$$\frac{\partial H'}{\partial t} + \frac{\partial(H'u_{\theta g})}{R\partial\theta} + \frac{\partial(H'u_{z g})}{\partial z} = 0 \tag{5}$$

$$\begin{aligned}
\rho H' \left(\frac{\partial u_{\theta g}}{\partial t} + u_{\theta g} \frac{\partial u_{\theta g}}{R\partial\theta} + u_{z g} \frac{\partial u_{\theta g}}{\partial z} \right) &= -H' \frac{\partial P_g}{R\partial\theta} - \frac{1}{2} \rho \lambda_{z g} u_{\theta g} u_{z g} \\
&\quad + \frac{1}{2} \rho 0.25 \lambda_f u_{z g} (u_{\theta d} - u_{\theta g})
\end{aligned} \tag{6}$$

$$\begin{aligned}
\rho H' \left(\frac{\partial u_{z g}}{\partial t} + u_{\theta g} \frac{\partial u_{z g}}{R\partial\theta} + u_{z g} \frac{\partial u_{z g}}{\partial z} \right) &= -H' \frac{\partial P_g}{\partial z} - \frac{1}{2} \rho u_{z g}^2 \cdot 0.25 \lambda_f \\
&\quad - \frac{1}{2} \rho \lambda_{z g} u_{z g}^2
\end{aligned} \tag{7}$$

Perturbation in eccentricity ratio ε is introduced to linearize the motion equations for the land part and the groove part. The zeroth-order perturbation equations describe a steady, zero-eccentricity flow condition and the first-order equations describe the pressure and flow conditions due to seal motion. Solutions for the first-order perturbation pressure p_1 lead to the definition of the seal dynamic coefficients, including direct stiffness, cross-coupled stiffness, direct damping, cross-coupled damping, and direct added mass.

Perturbation solutions for the land part

The governing Eq. [2], Eq. [3], and Eq. [4] for the land part are expanded in the perturbation variables

$$H = C_{l0} + \varepsilon \phi, \quad p = p_{l0} + \varepsilon p_1, \quad u_{z l} = u_{z l 0} + \varepsilon u_{z l 1}, \quad u_{\theta} = u_{\theta l 0} + \varepsilon u_{\theta l 1} \tag{8}$$

to yield the perturbation equations. The zeroth-order perturbation equations are solved analytically based on Hirs's turbulent lubrication theory by neglecting the changes in $u_{z l 0}$ along the axial direction. The zeroth-order circumferential-momentum and axial-momentum equations are as follows:

$$\frac{\partial u_{\theta l 0}}{\partial z} = -\frac{\lambda_{z l}}{C_{l0}} R\omega + \frac{\lambda_{z l}}{C} u_{\theta l 0} \tag{9}$$

$$C_{l0} \frac{\partial p_{l0}}{\partial z} = -\rho \lambda_{z l} u_{z l 0}^2 \tag{10}$$

It is assumed that $u_{\theta 10} = u_{\theta 1in}$ when $z=0$. Thus, the integration of Eq. [9] yields the relationship

$$u_{\theta 10} = (u_{\theta 1in} - a'R\omega)e^{-a'z} + a'R\omega \quad [11]$$

where $a' = -\lambda_{z1}/C_{10}$.

Substituting Eq. [8] into Eq. [2], Eq. [3], and Eq. [4] yields the first-order perturbation equations for the land part, including the continuity equation, the circumferential-momentum equation, and the axial-momentum equation. By ignoring the higher derivatives, the first-order perturbation equations can be simplified as follows:

$$\frac{C_{10}}{R} \frac{\partial u_{\theta 11}}{\partial \theta} + \left(\frac{\partial \phi}{\partial t} + \frac{1}{R} u_{\theta 10} \frac{L' \partial \bar{\phi}}{\partial \theta} \right) + C_{10} \frac{\partial u_{z11}}{\partial z} = 0 \quad [12]$$

$$\begin{aligned} & -\frac{C_{10}}{\rho R} \frac{\partial p_{11}}{\partial \theta} - \lambda_{z1} [u_{z11}(R\omega - u_{\theta 10}) - u_{z10} u_{\theta 11}] \\ & = C_{10} \frac{\partial u_{\theta 11}}{\partial t} + \frac{1}{R} C_{10} u_{\theta 10} \frac{\partial u_{\theta 11}}{\partial \theta} + C_{10} u_{\theta 10} \frac{\partial u_{\theta 11}}{\partial z} + C_{10} u_{z11} \frac{\partial u_{\theta 10}}{\partial z} + L' \bar{\phi} u_{z10} \frac{\partial u_{\theta 10}}{\partial z} \end{aligned} \quad [13]$$

$$\frac{\partial u_{z11}}{\partial t} + u_{\theta 10} \frac{\partial u_{z11}}{R \partial \theta} + u_{z10} \frac{\partial u_{z11}}{\partial z} = -\frac{\partial p_{11}}{\partial z} + \frac{\bar{\phi} L' \partial p_{10}}{C_{10} \partial z} - \frac{2\rho \lambda_{z1}}{C_{10}} u_{z11} u_{z10} \quad [14]$$

where $L' = L_1/\cos \alpha$ and the first-order perturbation terms u_{z11} , $u_{\theta 11}$, and p_{11} are all functions of z , t , and θ . Solutions for the preceding equations must satisfy the circumferential continuity conditions:

$$\begin{aligned} P_{11}(z, t, \theta) &= P_{11}(z, t, \theta + 2\pi) \\ u_{\theta 11}(z, t, \theta) &= u_{\theta 11}(z, t, \theta + 2\pi) \\ u_{z11}(z, t, \theta) &= u_{z11}(z, t, \theta + 2\pi) \end{aligned} \quad [15]$$

Thus, the following solution format is assumed

$$\begin{aligned} P_{11}(z, t, \phi) &= P_{11c}(z, t) \cos \theta + P_{11s}(z, t) \sin \theta \\ u_{\theta 11}(z, t, \phi) &= u_{\theta 11c}(z, t) \cos \theta + u_{\theta 11s}(z, t) \sin \theta \\ u_{z11}(z, t, \phi) &= u_{z11c}(z, t) \cos \theta + u_{z11s}(z, t) \sin \theta \end{aligned} \quad [16]$$

By introducing the complex variables shown in Eq. [17], the first-order perturbation circumferential-momentum equation, axial-momentum equation, and continuity equation can be obtained as Eq. [18], Eq. [19], and Eq. [20] respectively:

$$\begin{aligned} u_{z1} &= u_{z1c}(z, t) + i u_{z1s}(z, t) = u_{z11}(z) e^{i\Omega t} \\ u_{\theta 1} &= u_{\theta 1c}(z, t) + i u_{\theta 1s}(z, t) = u_{\theta 11}(z) e^{i\Omega t} \\ p_1 &= p_{1c}(z, t) + i p_{1s}(z, t) = p_{11}(z) e^{i\Omega t} \\ \phi &= -\frac{1}{\varepsilon} (x + iy) = \frac{R_0}{C_{10}} e^{i\Omega t} \end{aligned} \quad [17]$$

$$\begin{aligned} \frac{\partial u_{\theta 11}}{\partial z} + u_{z11} \cdot \left[\frac{1}{u_{z10}} \frac{\partial u_{\theta 10}}{\partial z} + \frac{1}{C_{10} u_{z10}} \lambda_{z1} (R\omega - u_{\theta 10}) \right] \\ + u_{\theta 11} \cdot \left(-\frac{\lambda_{z1}}{C_{10}} - i \frac{1}{R} \frac{u_{\theta 10}}{u_{z10}} + i \frac{\Omega}{u_{z10}} \right) - i \frac{1}{\rho R u_{z10}} \cdot p_{11} = \frac{R_0}{C_{10} \varepsilon} \frac{\partial u_{\theta 10}}{\partial z} \end{aligned} \quad [18]$$

$$\begin{aligned} \frac{\partial p_{11}}{\partial z} + u_{z10} \left[i \frac{u_{\theta 11}}{R} + i \frac{R_0}{C_{10} \varepsilon} \left(\Omega - \frac{u_{\theta 10}}{R} \right) \right] \\ + u_{z11} \left[i \left(\Omega - \frac{u_{\theta 10}}{R} \right) + \frac{2\rho \lambda_{z1}}{C_{10}} u_{z10} \right] = -\frac{R_0}{C_{10} \varepsilon} \cdot \frac{\partial p_{10}}{\partial z} \end{aligned} \quad [19]$$

$$\frac{\partial u_{z11}}{\partial z} - i \frac{1}{R} u_{\theta 11} = i \frac{R_0}{C_{10} \varepsilon} \left(\frac{\Omega}{C_{10}} - \frac{u_{\theta 10}}{C_{10} R} \right) \quad [20]$$

where Ω is the whirling velocity.

A nondimensional matrix equation demonstrated as Eq. [22] is obtained by introducing the variables

$$u_{\theta 11} = \bar{u}_{\theta 11} \cdot R\omega, \quad u_{z11} = \bar{u}_{z11} \cdot R\omega, \quad p_{11} = \rho u_{z10}^2 \bar{p}_{11} \quad [21]$$

into Eq. [18], Eq. [19], and Eq. [20]:

$$\frac{d}{dz} \begin{Bmatrix} \bar{u}_{1z1} \\ \bar{u}_{1\theta 1} \\ \bar{p}_{11} \end{Bmatrix} + [E] \begin{Bmatrix} \bar{u}_{1z1} \\ \bar{u}_{1\theta 1} \\ \bar{p}_{11} \end{Bmatrix} = \begin{Bmatrix} i \frac{R_0}{C_{10} \varepsilon} \frac{L'}{R\omega} \left(\frac{\Omega}{C_{10}} - \frac{u_{\theta 10}}{C_{10} R} \right) \\ \frac{L'}{R\omega} \cdot \frac{R_0}{C_{10} \varepsilon} \cdot \frac{\partial u_{\theta 10}}{\partial z} \\ -\frac{R_0}{C_{10} \varepsilon} \cdot \frac{\partial p_{10}}{\partial z} - i \frac{1}{\rho u_{z10}^2} \cdot \frac{R_0}{C_{10} \varepsilon} \left(\Omega - \frac{u_{\theta 10}}{R} \right) \end{Bmatrix} \quad [22]$$

where $E_{11} = E_{13} = E_{33} = 0$, $E_{12} = -i \frac{1}{R} L'$, $E_{32} = \frac{\omega}{\rho u_{z10}}$,

$$E_{21} = L' \left[\frac{1}{u_{z10}} \frac{\partial u_{\theta 10}}{\partial z} + \frac{1}{C_{10} u_{z10}} \lambda_{z1} (R\omega - u_{\theta 10}) \right],$$

$$E_{31} = \frac{1}{\rho u_{z10}^2} R\omega \left[i \left(\Omega - \frac{u_{\theta 10}}{R} \right) + \frac{2\rho \lambda_{z1}}{C_{10}} u_{z10} \right],$$

$$E_{22} = L' \cdot \left(-\frac{\lambda_{z1}}{C_{10}} - i \frac{1}{R} \frac{u_{\theta 10}}{u_{z10}} + i \frac{\Omega}{u_{z10}} \right), \text{ and } E_{23} = -i \frac{L'}{R\omega} \cdot \frac{u_{z10}^2}{R u_{z10}}.$$

The following three boundary conditions for the land part are specified for the solution of Eq. [22]:

a. The exit first-order perturbation pressure is zero, that is,

$$\bar{p}_{11}(1) = 0 \quad [23]$$

b. The entrance first-order perturbation circumferential velocity is zero, that is,

$$\bar{u}_{\theta 11}(0) = 0 \quad [24]$$

c. The pressure-loss-induced boundary conditions at the entrance is simplified as

$$\bar{p}_{11}(0) = -R\omega(1 + \xi_{zin}) \bar{u}_{z11}(0) / u_{z10} \quad [25]$$

A series of numerical solutions for \bar{u}_{z11} , $\bar{u}_{\theta 11}$, and \bar{p}_{11} can be acquired by solving Eq. [22] using the target method and Newton-Raphson method combined with the boundary conditions. Thus, the first-order pressure distribution within the land part along the axial direction can be obtained and be expressed as

$$\bar{p}_{11}(z) = \left(\frac{r_0}{\varepsilon} \right) [f_{1c}(z) + i f_{1s}(z)] \quad [26]$$

The flow-induced force components acting on the rotor due to shaft motion are represented as

$$F_{xl}(t) = -\varepsilon RL' \rho u_{z0}^2 \sum_{n=1}^{I_s} \left[(I_s \cdot L_s - 1) \int_{\varphi_n}^{\varphi_{n+1/2}} \int_0^1 f_{1c} \cos \varphi \, dz d\varphi \right. \\ \left. + I_s \cdot L_s \int_{\varphi_{n+1/2}}^{\varphi_{n+1}} \int_0^1 f_{1c} \cos \varphi \, dz d\varphi \right] \quad [27]$$

$$F_{yl}(t) = -\varepsilon RL' \rho u_{z0}^2 \sum_{n=1}^{I_s} \left[(I_s \cdot L_s - 1) \int_{\varphi_n}^{\varphi_{n+1/2}} \int_0^1 f_{1s} \sin \varphi \, dz d\varphi \right. \\ \left. + I_s \cdot L_s \int_{\varphi_{n+1/2}}^{\varphi_{n+1}} \int_0^1 f_{1s} \sin \varphi \, dz d\varphi \right] \quad [28]$$

Definition of the flow-induced forces can be simplified by performing the integration at a time when the rotating displacement vector is pointing along the X axis, that is, when $t=0$. At this time, F_{xl} and F_{yl} are both functions of Ω for the reason that f_{1c} and f_{1s} are functions of Ω . Moreover, at this time, the force components F_{xl} and F_{yl} are equal to the radial force component F_{rl} and circumferential force component $F_{\theta l}$, respectively, which can be expressed as

$$-F_{xl} = -F_{rl} = \varepsilon [K_l + 120\pi c_l \Omega - M_l (120\pi \Omega)^2] \quad [29]$$

$$-F_{yl} = -F_{\theta l} = \varepsilon (k_l + 120\pi C_l \Omega) \quad [30]$$

Substitution from Eq. [27] and Eq. [28] yields

$$-\varepsilon RL' \rho u_{z0}^2 \sum_{n=1}^{I_s} \left[(I_s \cdot L_s - 1) \int_{\varphi_n}^{\varphi_{n+1/2}} \int_0^1 f_{1c} \cos \varphi \, dz d\varphi + I_s \cdot L_s \right. \\ \left. \times \int_{\varphi_{n+1/2}}^{\varphi_{n+1}} \int_0^1 f_{1c} \cos \varphi \, dz d\varphi \right] = -\varepsilon [K_l + 120\pi c_l \Omega - M_l (120\pi \Omega)^2] \quad [31]$$

$$\varepsilon RL' \rho u_{z0}^2 \sum_{n=1}^{I_s} \left[(I_s \cdot L_s - 1) \int_{\varphi_n}^{\varphi_{n+1/2}} \int_0^1 f_{1s} \sin \varphi \, dz d\varphi + I_s \cdot L_s \right. \\ \left. \times \int_{\varphi_{n+1/2}}^{\varphi_{n+1}} \int_0^1 f_{1s} \sin \varphi \, dz d\varphi \right] = \varepsilon (k_l + 120\pi C_l \Omega) \quad [32]$$

Hence, the dynamic coefficients (K_l , k_l , C_l , c_l , M_l) can be calculated by first evaluating the left-hand side of Eq. [31] and Eq. [32] for the frequency set (Ω/ω : 0, 0.5, 1.0, 1.5, 2.0), then performing a least-square calculation.

Perturbation solutions for the groove part

By introducing perturbation variables shown in Eq. [8] into Eq. [5], Eq. [6], and Eq. [7], the first-order perturbation equations for the groove part including the continuity equation, the circumferential-momentum equation, and the

axial-momentum equation are obtained and shown as Eq. [33], Eq. [34], and Eq. [35]:

$$\frac{C_{g0}}{R} \frac{\partial u_{\theta g1}}{\partial \theta} + \left(\frac{\partial \phi}{\partial t} + \frac{1}{R} u_{\theta g0} \frac{L''}{\partial \theta} \right) + C_{g0} \frac{\partial u_{zg1}}{\partial z} = 0 \quad [33]$$

$$-\frac{C_{g0}}{\rho R} \frac{\partial P_{g1}}{\partial \theta} - \frac{1}{2} \lambda_{ga} [u_{zg1} u_{\theta g0} + u_{zg0} u_{\theta g1}] \\ + \frac{1}{2} 0.25 \lambda_f [u_{zg0} u_{\theta g1} + u_{zg1} (u_{d0} - u_{\theta g0})] \\ = C_{g0} \frac{\partial u_{\theta g1}}{\partial t} + \frac{1}{R} C_{g0} u_{\theta g0} \frac{\partial u_{\theta g1}}{\partial \theta} + C_{g0} u_{\theta g0} \frac{\partial u_{\theta g1}}{\partial z} \quad [34]$$

$$\frac{\partial u_{zg1}}{\partial t} + u_{\theta g0} \frac{\partial u_{zg1}}{R \partial \theta} + u_{zg0} \frac{\partial u_{zg1}}{\partial z} = -\frac{\partial P_{g1}}{\partial z} - \frac{\bar{\phi} L''}{C_{g0}} \frac{\partial P_{g0}}{\partial z} \\ - \frac{\rho}{2C_{g0}} u_{zg1} u_{zg0} (0.25 \lambda_f + \lambda_{zg}) \quad [35]$$

where $L'' = L_g / \cos \alpha$.

Nondimensional matrix equations for the groove part are obtained by introducing complex variables and nondimensional variables that are similar to those shown in Eq. [17] and Eq. [21] for the land part. The matrix equations are shown:

$$\frac{d}{dz} \begin{Bmatrix} \bar{u}_{gz1} \\ \bar{u}_{g\theta1} \\ \bar{P}_{g1} \end{Bmatrix} + [F] \begin{Bmatrix} \bar{u}_{gz1} \\ \bar{u}_{g\theta1} \\ \bar{P}_{g1} \end{Bmatrix} = \begin{Bmatrix} i \frac{R_0}{C_{g0} \varepsilon} \frac{L''}{R \omega} \left(\frac{\Omega}{C_{g0}} - \frac{u_{\theta g0}}{C_{l0} R} \right) \\ 0 \\ -\frac{R_0}{C_{g0} \varepsilon} \cdot \frac{\partial P_{l0}}{\partial z} - i \frac{1}{\rho u_{zg0}^2} \cdot \frac{R_0}{C_{g0} \varepsilon} \left(\Omega - \frac{u_{\theta g0}}{R} \right) \end{Bmatrix} \quad [36]$$

where $F_{11} = F_{13} = F_{33} = 0$, $F_{12} = -i \frac{1}{R} L''$, $F_{32} = \frac{\omega}{\rho u_{g0}}$, $F_{22} = L'' \cdot \left[-\frac{u_{zg0}}{2C_{g0}} (\lambda_{zg} - 0.25 \lambda_f) - i \left(\frac{1}{R} \frac{u_{\theta g0}}{u_{zg0}} - \frac{\Omega}{u_{zg0}} \right) \right]$, $F_{21} = \frac{L''}{R \omega} \cdot \frac{1}{2C_{g0} u_{zg0}} [\lambda_{zg} - 0.25 \lambda_f (u_{dm} - u_{\theta g0})] + i \left(\frac{\Omega L''}{u_{\theta g0} R \omega} - \frac{L''}{R^2 \omega} \right)$, $F_{31} = \frac{1}{\rho u_{zg0}^2} R \omega \left[i \left(\Omega - \frac{u_{\theta g0}}{R} \right) + \frac{\rho (\lambda_{zg} + 0.25 \lambda_f)}{2C_{g0}} u_{zg0} \right]$, and $F_{23} = -i \frac{L''}{R \omega} \cdot \frac{u_{zg0}^2}{R u_{\theta g0}}$.

Boundary conditions demonstrated in Eq. [37] are used to solve the matrix equation of the groove part:

$$\bar{p}_{g1}(1) = 0, \quad \bar{u}_{\theta g1}(0) = 0, \quad \bar{p}_{g1}(0) = -R \omega (1 + \zeta_{zin}) \bar{u}_{zg1}(0) / u_{zg0} \quad [37]$$

First-order pressure distribution within the groove part along the axial direction can be obtained and be expressed as

$$\bar{p}_{g1}(z) = \left(\frac{r_0}{\varepsilon} \right) [f_{2c}(z) + i f_{2s}(z)] \quad [38]$$

The flow-induced force components acting on the rotor due to shaft motion are represented as

$$F_{xg}(t) = -\varepsilon RL'' \rho u_{zg0}^2 \sum_{n=1}^{I_s} \left[(I_s \cdot L_s - 1) \int_{\varphi_n}^{\varphi_{n+1/2}} \int_0^1 f_{2c} \cos \varphi \, dz d\varphi \right. \\ \left. + I_s \cdot L_s \int_{\varphi_{n+1/2}}^{\varphi_{n+1}} \int_0^1 f_{2c} \cos \varphi \, dz d\varphi \right] \quad [39]$$

$$F_{yg}(t) = -\varepsilon RL'' \rho u_{zg0}^2 \sum_{n=1}^{I_s} \left[(I_s \cdot L_s - 1) \int_{\varphi_n}^{\varphi_{n+1/2}} \int_0^1 f_{2s} \sin \varphi \, dz d\varphi \right. \\ \left. + I_s \cdot L_s \int_{\varphi_{n+1/2}}^{\varphi_{n+1}} \int_0^1 f_{2s} \sin \varphi \, dz d\varphi \right] \quad [40]$$

Similar to the solution method of the land part, a set of equations for the whirling velocity Ω can be obtained as Eq. [41] and Eq. [42]. The dynamic coefficients for the groove part (K_g , k_g , C_g , c_g , M_g) can also be calculated by first evaluating the left-hand side of Eq. [41] and Eq. [42] for the frequency set (Ω/ω : 0, 0.5, 1.0, 1.5, 2.0) and performing a least-square calculation:

$$-\varepsilon RL'' \rho u_{zg0}^2 \sum_{n=1}^{I_s} \left[(I_s \cdot L_s - 1) \int_{\varphi_n}^{\varphi_{n+1/2}} \int_0^1 f_{2c} \cos \varphi \, dz d\varphi + I_s \cdot L_s \right. \\ \left. \times \int_{\varphi_{n+1/2}}^{\varphi_{n+1}} \int_0^1 f_{2c} \cos \varphi \, dz d\varphi \right] = -\varepsilon \left[K_g + 120\pi c_g \Omega - M_g (120\pi \Omega)^2 \right] \quad [41]$$

$$-\varepsilon RL'' \rho u_{zg0}^2 \sum_{n=1}^{I_s} \left[(I_s \cdot L_s - 1) \int_{\varphi_n}^{\varphi_{n+1/2}} \int_0^1 f_{2s} \sin \varphi \, dz d\varphi + I_s \cdot L_s \right. \\ \left. \times \int_{\varphi_{n+1/2}}^{\varphi_{n+1}} \int_0^1 f_{2s} \sin \varphi \, dz d\varphi \right] = \varepsilon (k_g + 120\pi C_g \Omega) \quad [42]$$

Rotordynamic characteristics of SGLS

The rotordynamic coefficient matrix of a spiral-grooved liquid seal represents the summation of the coefficients of the land and the groove part. A calculation program is developed based on the numerical method proposed in this article. Figure 3 illustrates the main sequential steps of the procedure.

Numerical example and discussion

Most experimental research on the characteristics of spiral-grooved seals focused on the seals with grooves on the stator, including the experimental work by Kanki (15), Childs (17–19), and Nagai (11). Among these researchers, Iwatubo (16) conducted a series of experiments on the leakage rates and dynamic characteristics for six spiral-grooved seals,

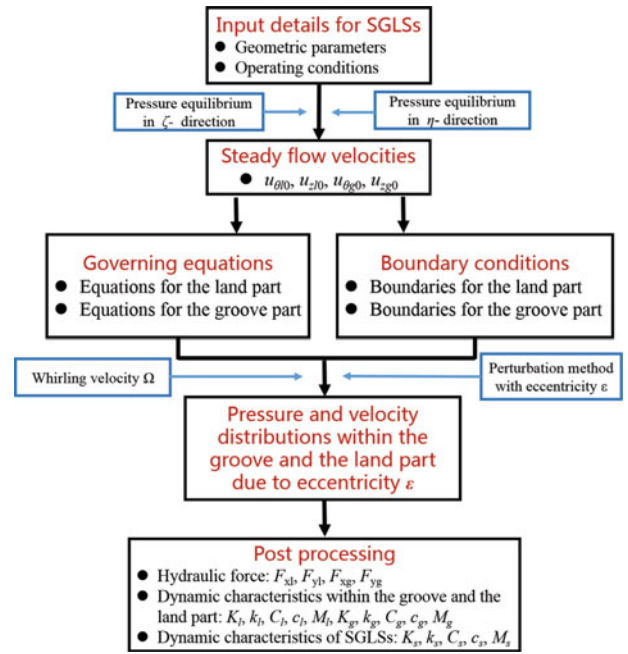


Figure 3. Program flow chart.

including one with the grooves on the rotor. The test rig and the measurement method of Iwatubo are quite different from those of the Texas A&M turbomachinery laboratory. In his apparatus, two ball bearings are used to yield the rotating and whirling motions of the rotor. An inside sleeve and an outside sleeve that have 0.05mm eccentricity to each other are attached between the two bearings. By rotating the two eccentric sleeves relatively, an arbitrary whirling amplitude can be adjusted in the range of 0mm to 0.1mm. The sleeves of both sides are synchronously driven by a motor through timing belts to obtain a whirling motion. The whirling speeds and their directions are controlled by an electric inverter. The rotating speed and the direction of the rotor can also be changed by the other motor controlled by an electric inverter (35). Variables such as rotating speed, whirling speed, pressure, leakage flow rate, and displacement of the rotor are obtained by the measuring system. Most importantly, the fluid forces acting on the stator are measured by load cells. The dynamic characteristics can be calculated by the measured forces under different whirling speeds. In the present analysis, comparisons are conducted between the experimental results of Iwatubo and the theoretical solutions to verify the analysis method presented in this article. The detailed geometric parameters of the model seal, working fluid properties, and operating conditions are demonstrated in Table 1.

Figure 4 compares the measured and predicted leakage rates of the model seal at different rotating speeds. It is observed that the predicted leakage rate decreases substantially with the increasing rotating speed, which is in accordance with the experimental results. However, the prediction error increases from 1.6% to 9% with the rotating speed. This consistent discrepancy is due to the influence of convective inertial effects, which is one of the predominant factors causing groove–land discontinuities and is neglected in

Table 1. Geometric parameters and operating conditions of the model SGLS.

Item	Value
Rotor diameter (mm)	70.5
Radial clearance (mm)	0.175
Seal length (mm)	35.25
Groove depth (mm)	1.2
Groove width (mm)	1.6
Land width (mm)	1.6
Number of thread	4
Spiral angle (°)	3.32
Dynamic viscosity (mPa·s)	1.009
Fluid density (kg/m ³)	1000
Kinematic viscosity (m ² /s)	1.006×10^{-6}
Pressure difference (MPa)	0.588
Rotating speed (rev/min)	500–3500

the steady-flow characteristics analysis in Vohr's equations (2). In essence, these inertial effects cause a sharp reduction in pressure when the flow exits from the deeper groove region into its narrower land region, while most of the pressure loss is not recovered when the flow exits from the land region into the next groove. Therefore, the spiral grooves have a larger effective resistance to flow than the predicted one considering turbulent flow shear resistance alone, which results in the overestimated leakage flow.

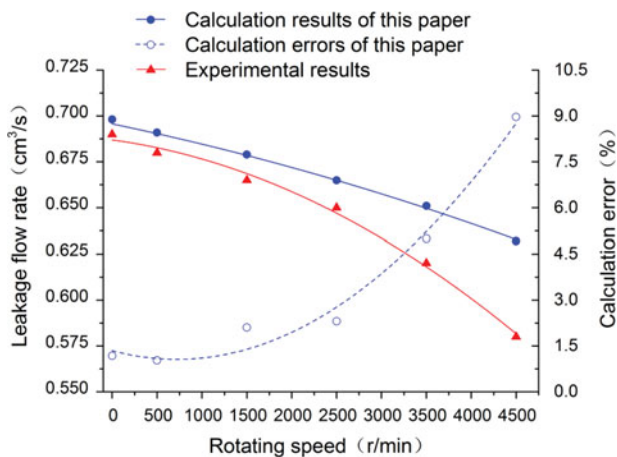
Figures 5a, 5b, 5c, 5d, and 5e illustrate the direct stiffness, cross-coupled stiffness, direct damping, cross-coupled damping, and direct added mass changes with the increasing rotating speed, respectively. Experimental results, prediction results of Iwatsubo, and the results using the proposed solution method of this article are also compared in Figure 5.

It is observed in Figure 5a that the rotating speed has little influence on the changes of the direct stiffness coefficient. Both the solution method proposed in this article and the method of Iwatsubo overpredict the direct stiffness value. The maximum discrepancy between the experimental results and the predicted results of this article is within 9%, while the discrepancies of Iwatsubo are more than 20%. Compared to the direct stiffness, cross-coupled stiffness is more sensitive to the changes of rotating speed, as shown in Figure 5b. The experimental results of cross-coupled stiffness and the predicted ones of this article show a parabolic increase with the rotating speed; however, the results of Iwatsubo show a linear change. Besides, the growth rate of

experimental results is much faster than the results based on the two solution methods. The minimum errors of both solution methods occur at the rotating speed of 1000rpm, and the errors become larger with increasing rotating speed. As illustrated in Figure 5c, the measured direct damping coefficients show a 16% increase as the rotating speed is raised from 500 rev/min to 3500 rev/min. However, the calculation values of Iwatsubo remain around 295N·s/m and the calculation results of the authors' method decrease with the increasing speed. The calculation results of both methods are always smaller than the experimental ones in the shown examples. Besides, the proposed method in this article has higher calculation accuracy of direct damping at lower rotating speed. The increasing discrepancies with rotating speed between experimental and theoretical cross-coupled stiffness and direct damping are probably because of the changes of circumferential Reynolds number and inlet flow conditions. Essentially, the cross-coupled stiffness coefficient k yields a "driving" tangential contribution in the direction of rotation, while the direct damping coefficient C develops a drag force opposing the tangential velocity. Both coefficients are sensitive to circumferential variables, especially the circumferential Reynolds number and preswirl velocity. As the rotational speed increases, the preswirl effects are gradually strengthened, causing a substantial increase in preswirl speed, which is one of the key factors affecting cross-coupled stiffness coefficients.

It is also indicated in Figure 5d that both the measured cross-coupled damping coefficients and the predicted results of this article are negative, and change little with the rotating speed. The calculation results of Iwatsubo are positive, and are more sensitive to the changes of rotating speed. Besides, the absolute values of the coefficients calculated using the method proposed in this article are much closer to the experimental results, compared to the calculation values of Iwatsubo. Through the comparisons with experimental results, it is obvious that both theoretical methods failed to predict the added mass coefficients. The measured values are almost two orders of magnitude larger than the theoretical ones, as shown in Figure 5e. This is probably because except for the inertia added mass generated by the seal, the experimental mass terms contain the contribution of the fluid in the test stator entrance and discharge chambers.

Figure 6 and Fig. 7, which compare the experimental force coefficients F_r/ε and F_θ/ε , which can be calculated from Eqs. [29] and [30] with predicted results using two methods, are illustrated as supplementary proofs of the analysis method proposed in this article. It is shown in Fig. 6 that the radial force coefficient F_r/ε changes little with the increasing rotating speed at a whirling speed of 600 rev/min. And the changing trends of the experimental and theoretical force coefficient are all consistent well with trends of the direct stiffness. That's because in this calculation model, the direct stiffness contributes nearly 90% to the radial force, which is in line with its definition of describing the magnitude of radial support. Compared with the measured circumferential forces, both theoretical analysis methods underestimate the variation of circumferential force with

**Figure 4.** Leakage flow rate versus rotating speed.

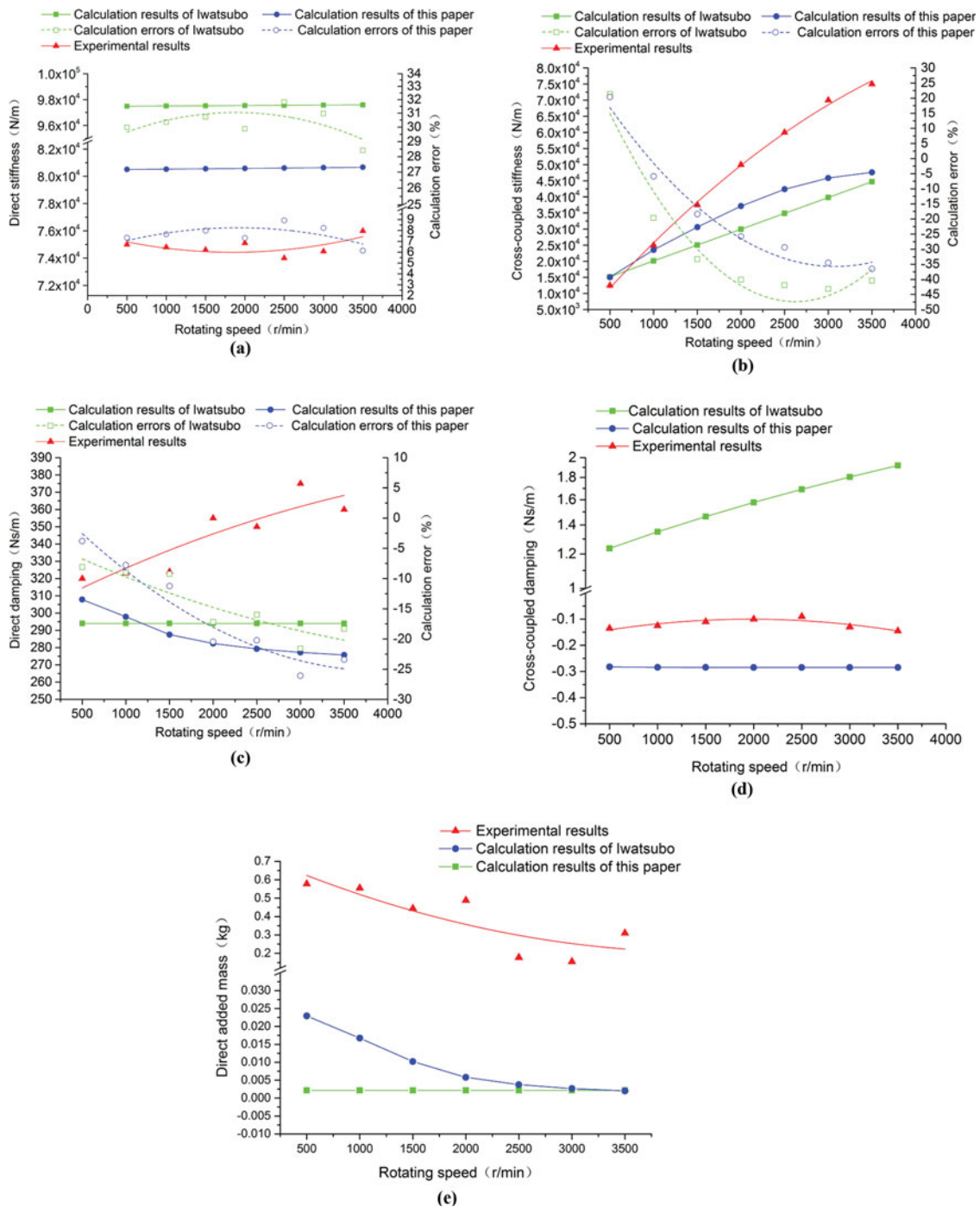


Figure 5. (a) Direct stiffness versus rotating speed. (b) Cross-coupled stiffness versus rotating speed. (c) Direct damping versus rotating speed. (d) Cross-coupled damping versus rotating speed. (e) Direct added mass versus rotating speed.

rotating speed. Referring to the composition equation of circumferential force shown as Eq. [30], it can be drawn that the cross stiffness and direct damping have equivalent effects on the magnitude of circumferential force. However, with the increase of whirling speed, direct damping will become the dominant factor. As can be seen from Figure 7, calculated circumferential force coefficients F_{θ}/ϵ at a rotating speed of 500r/min agree well with the measured ones, showing a linearly decrease as the Ω/ω ratio increases. Note that the predicted radial force coefficient F_{ρ}/ϵ using the present

method shows the same qualitative tendencies with the measured results as the whirling speed changes. The coefficient decreases first with the decreasing backward whirling speed, then increases with the increasing forward whirling speed. However, Iwatsubo's solution results show an opposite change with the increasing forward whirling speed.

In general, compared to the theoretical results of Iwatsubo, the present analysis method leads to an improved accuracy of stiffness, damping, and hydraulic force prediction, especially for the circumferential variables and the

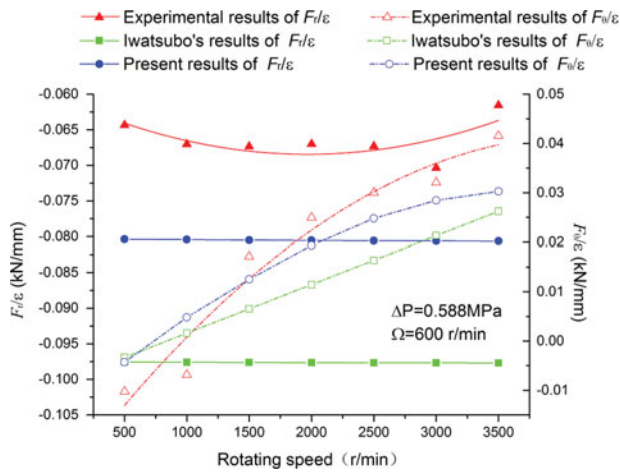


Figure 6. Effects of rotating speed on force coefficients F_r/ϵ and F_θ/ϵ .

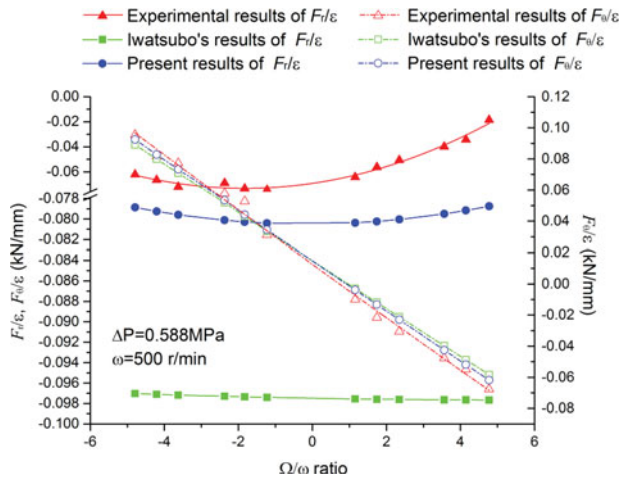


Figure 7. Force coefficients F_r/ϵ and F_θ/ϵ versus speed ratio Ω/ω .

variables related to them. This improvement is largely due to the better description of the fluid flow within the seal clearance. In fact, the circumferential shear stresses caused by the inlet prerotation and the rotation of the shaft will motivate the whirling motion of the rotor, then affect the flow field details such as velocity and pressure distribution within the seal clearance, and finally affect the hydraulic forces and equivalent dynamic characteristics of the seal. Therefore, the governing equations considering circumferential momentum equation and circumferential velocity perturbation terms lead to more accurate pressure distribution, hydraulic forces, and equivalent dynamic characteristics.

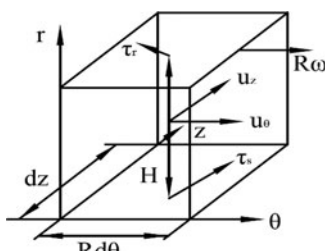


Figure 8. Spiral-grooved seal differential element.

Conclusion

A theoretical analysis method for leakage flow rate and dynamic characteristics of spiral-grooved liquid seals is proposed based on the studies of Iwatsubo (5) and Childs (32). In this method, governing equations and the solutions taking account of the circumferential velocity perturbation change with the axial location of the land part and the groove part are respectively built. Moreover, the accuracy of the analytical method was verified by comparison with the experimental results conducted by Iwatsubo, including leakage rates, direct stiffness, cross-coupled stiffness, direct damping, cross-coupled damping, direct added mass coefficients, radial force, and circumferential force coefficients. According to the comparisons, the trends of the theoretical and experimental stiffness coefficients are consistent. The present analytical method overpredicts the leakage flow rate with an error of less than 10%. The predicted direct stiffness and cross-coupled stiffness of the present solution method correlate well with the experimental evidence. The predicted direct damping coefficients of this article show an opposite change with the rotating speed compared to the experimental results with a maximum error of 27%. Besides, the calculation accuracy of cross-coupled damping is raised substantially compared to the solution method of Iwatsubo.

Funding

This work was supported by the National Natural Science Foundation of China (Grant 51606170), Zhejiang Province public welfare technology research project (Grant 2017C31045), and Science Foundation of Zhejiang Sci-Tech University (ZSTU) under Grant 15022083-Y.

References

- (1) Chow, C. Y., and Vohr, J. H. (1970), "Helical-Grooved Journal Bearing Operated in Turbulent Regime," *Journal of Lubrication Technology*, **92**(2), pp 346–357.
- (2) Vohr, J. H., and Chow, C. Y. (1969), "Theoretical Analysis of Spiral-Grooved Screw Seal for Turbulent Operation," *Journal of Lubrication Technology*, **91**(4), pp 675–686.
- (3) Zuk, J., Strom, T. N., Ludwig, L. P., and Johnson, R. L. (1967), "Convective Inertia and Gas Ingestion Effects on Flow Regimes of the Viscoseal Theory and Experiment," *ASLE Transactions*, **10**(3), pp 273–293.
- (4) Iwatsubo, T., Yang, B., and Ibaraki, R. (1986), "Static and Dynamic Characteristics of Parallel-Grooved Seals," *Proceedings of Rotordynamic Instability Problems in High Performance Turbomachinery*, NASA CP-2443, Texas A&M University, pp 99–127.
- (5) Iwatsubo, T., Yang, B., and Ibaraki, R. (1986), "Theoretical Approach to Obtaining Dynamic Characteristics of Noncontacting Spiral-Grooved Seals," *Proceedings of Rotordynamic Instability Problems in High Performance Turbomachinery*, NASA CP-2443, Texas A&M University, pp 155–188.
- (6) Iwatsubo, H., Nishino, T., and Ishimaru, H. (1996), "A Study on Dynamic Characteristics of Double Spiral Grooved Seals," *Proceedings of Rotordynamic Instability Problems in High Performance Turbomachinery*, NASA CP-3344, pp 113–134.
- (7) Nordmann, R., Dietzen, F. J., Janson, W., et al. (1986), "Rotordynamic Coefficients and Leakage Flow of Parallel Grooved Seals and Smooth Seals," NASA, Lewis Research

- Center Rotordynamic Instability Problems in High-Performance Turbomachinery, pp 129–153.
- (8) Kim, C. H., and Childs, D. W. (1987), “Analysis for Rotordynamic Coefficients of Helically-Grooved Turbulent Annular Seals,” *ASME Journal of Tribology*, **109**(1), pp 136–143.
- (9) Florjancic, S. (1990), “Annular Seals of High Energy Centrifugal Pumps: A New Theory and Full Scale Measurement of Rotordynamic Coefficients and Hydraulic Friction Factors,” Doctoral Thesis, Swiss Federal Institute of Technology, Switzerland.
- (10) Marquette, O. R., and Childs, D. W. (1996), “An Extended Three-Control-Volume Theory for Circumferentially-Grooved Liquid Seals,” *ASME Journal of Tribology*, **118**(2), pp 276–285.
- (11) Nagai, K., Kaneko, S., Taura, H., and Watanabe, Y. (2018), “Numerical and Experimental Analyses of Static Characteristics for Liquid Annular Seals With Helical Grooves in Seal Stator,” *Journal of Tribology*, **140**(3), p 032201.
- (12) Pape, J. G., and Vrakking, W. J. (1968), “Viscoseal—Pressure Generation and Friction Loss under Turbulent Conditions,” *ASLE Transactions*, **11**, 4, pp 310–320.
- (13) Ketola, H. N., and McGrew, J. M. (1967), “Turbulent Operation of the Visco Seal,” *ASLE Transactions*, **10**(3), pp 256–272.
- (14) Stair, W. K. (1967), “Turbulent Visco Seal—Theory and Experiment,” *Proceedings of 3rd International Conference on Fluid Sealing, British Hydromechanics Research Association*, Cambridge, England, pp H2–H21.
- (15) Kanki, H., and Kawakami, T. (1988), “Experimental Study on the Static and Dynamic Characteristics of Screw Grooved Seals,” *ASME Journal of Vibration and Acoustics*, **110**(3), pp 326–331.
- (16) Iwatsubo, T., Sheng, B. C., and Ono, M. (1990), “Experiment of Static and Dynamic Characteristics of Spiral Grooved Seals,” *Proceedings of the Sixth Workshop on Rotordynamic Instability Problems in High-Performance Turbomachinery*, pp 223–233.
- (17) Childs, D. W. (1983), “SSME Seal Test Program: Leakage Tests for Helically-Grooved Seals,” NASA Progress Report, No. 8–33716.
- (18) Childs, D. W., Nolan, S. A., and Kilgore, J. J. (1990), “Test Results for Turbulent Annular Seals, Using Smooth Rotors and Spiral Grooved Stators,” *ASME Journal of Tribology*, **112**(2), pp 254–258.
- (19) Childs, D. W., and Gansle, A. J. (1995, June), “Experimental Leakage and Rotordynamic Results for Helically Grooved Annular Gas Seals,” *ASME 1995 International Gas Turbine and Aeroengine Congress and Exposition*, pp V005T14A009–V005T14A009.
- (20) Proctor, M. P., and Delgado, I. R. (2008), “Preliminary Test Results of a Non-Contacting Finger Seal on a Herringbone-Grooved Rotor,” NASA Technical Memorandum, 2008–215475.
- (21) Bhattacharya, A. (1997), “CFD Based Rotordynamics Coefficients for Labyrinth Seals and Impeller Shroud Leakage Paths,” MS Thesis, Texas A&M University, College Station, TX.
- (22) Nielsen, K. K., Jønck, K., and Underbakke, H. (2012), “Hole-Pattern and Honeycomb Seal Rotordynamic Forces: Validation of CFD-Based Prediction Techniques,” *ASME Journal of Engineering for Gas Turbines and Power*, **134**(12), pp 122505.
- (23) Gao, R., and Kirk, G. (2013), “CFD Study on Stepped and Drum Balance Labyrinth Seal,” *Tribology Transactions*, **56**(4), pp 663–671.
- (24) Kirk, G., and Gao, R. (2012), “Influence of Preswirl on Rotordynamic Characteristics of Labyrinth Seals,” *Tribology Transactions*, **55**(3), pp 357–364.
- (25) Gao, R. (2012), “Computational Fluid Dynamic and Rotordynamic Study on the Labyrinth Seal,” Doctoral Thesis, Virginia Polytechnic Institute and State University, Blacksburg, VA.
- (26) Untaroiu, A., Untaroiu, C. D., Wood H. G., et al. (2013), “Numerical Modeling of Fluid-Induced Rotordynamic Forces in Seals With Large Aspect Ratios,” *ASME Journal of Engineering for Gas Turbines and Power*, **135**(1), 012501
- (27) Untaroiu, A., Hayrapetian, V., Untaroiu, C. D., et al. (2013), “On the Dynamic Properties of Pump Liquid Seals,” *ASME Journal of Fluids Engineering*, **135**(5), pp 051104.
- (28) Chochua, G., and Soulas, T.A. (2007), “Numerical Modeling of Rotordynamic Coefficients for Deliberately Roughened Stator Gas Annular Seals,” *ASME Journal of Tribology*, **129**(2), pp 424–429.
- (29) Yan, X., Li, J., and Feng, Z. (2011), “Investigations on the Rotordynamic Characteristics of a Hole-Pattern Seal Using Transient CFD and Periodic Circular Orbit Model,” *ASME Journal of Vibration and Acoustics*, **133**(4), pp 041007.
- (30) Nielsen, K. K., Jønck, K., and Underbakke, H. (2012), “Hole-Pattern and Honeycomb Seal Rotordynamic Forces: Validation of CFD-Based Prediction Techniques,” *ASME Journal of Engineering for Gas Turbines and Power*, **134**(12), pp 122505.
- (31) Subramanian, S., Sekhar, A. S., and Prasad, B. (2016), “Rotordynamic Characteristics of Rotating Labyrinth Gas Turbine Seal With Centrifugal Growth,” *Tribology International*, **97**, pp 349–359.
- (32) Childs, D. W. (1983), “Finite-Length Solutions for Rotordynamic Coefficients of Turbulent Annular Seals,” *Journal of Lubrication Technology*, **105**(3), pp 437–444.
- (33) Childs, D. W. (1993), *Turbomachinery Rotordynamics: Phenomena, Modeling, and Analysis*, John Wiley & Sons: New York, NY.
- (34) Hirs, G. G. (1974), “A Systematic Study of Turbulent Film Flow,” *Journal of Lubrication Technology*, **96**(1), pp 118–126.
- (35) Kanemori, Y., and Iwatsubo, T. (1992), “Experimental Study of Dynamic Fluid Forces and Moments for a Long Annular Seal,” *Journal of Tribology*, **114**(4), pp 773–778.

Appendix A

Steady flow characteristics of spiral-grooved liquid annular seal

An adequate discussion of the steady flow characteristics of spiral-grooved seal is conducted in Iwatsubo et al. (5). Most of the main equations used in the present analysis are demonstrated in this appendix. Vohr’s theoretical analysis and experimental analysis for spiral grooves are used to describe the pumping effects in Iwatsubo’s theory. The equivalent pressure induced by the turbulent pumping flows is as follows:

$$\Delta P_{\text{pumping}} = 0.0159Re_l^{0.778} \cdot \frac{6\mu R\omega L_s}{C_{l0}^2} \cdot \frac{L_{lg}(1 - L_{lg})(K_e^3 - 1)(K_e - 1)\tan\alpha}{K_e^3(1 + \tan^2\alpha) + L_{lg}(1 - L_{lg})(K_e^3 - 1)^2\tan^2\alpha} \quad (A.1)$$

where $L_{lg} = L_l/(L_l + L_g)$, $K_e = T/(T + C_{l0})$. The preceding equivalent pressure difference due to turbulent pumping action is reported to be accurate to within 5% when overall Reynolds number within the seal clearance is above 5000 and the grooves parameters are preferably subject to the conditions that $\alpha \leq 15^\circ$, $C_{l0}/(C_{l0} + T) > 3.6$, and $0.2 < L_g/(L_g + L_l) < 0.8$.

Pressure equilibrium in the η -direction within the land region:

$$P - \Delta P_{\text{pumping}} = \frac{1}{2}\rho(1 + \xi_{\eta in})u_{\eta 0}^2 + \frac{1}{2}\rho(1 - \xi_{\eta out})u_{\eta 0}^2 + \frac{1}{2}\rho\lambda_{\eta}u_{\eta 0}^2 \frac{2L_s}{C_{l0}\sin\alpha} \quad (A.2)$$

Pressure equilibrium in the ζ -direction within the groove region:

$$P - \Delta P_{\text{pumping}} = \frac{1}{2}\rho(1 + \xi_{\zeta in})u_{\zeta 0}^2 + \frac{1}{2}\rho(1 - \xi_{\zeta out})u_{\zeta 0}^2 + \frac{1}{2}\rho\lambda_{\zeta}u_{\zeta 0}^2 \frac{L_g}{R_{equ} \cdot \sin\alpha} \quad (A.3)$$

where $R_{equ} = L_g(C_{l0} + T)/2(L_g + C_{l0} + T)$.

The steady flow velocities in axial and circumferential directions $u_{\theta l0}$, $u_{z l0}$, $u_{\theta g0}$, and $u_{z g0}$ are obtained from the previous calculation results of $u_{\eta l0}$, $u_{\zeta l0}$, and $u_{\eta g0}$ by coordinate translation shown here:

$$\begin{aligned} u_{\theta l0} &= R\omega - u_{\eta l0}\cos\alpha + u_{\zeta l0}\sin\alpha & u_{z l0} &= u_{\eta l0}\sin\alpha + u_{\zeta l0}\cos\alpha \\ u_{\theta g0} &= R\omega - u_{\eta g0}\cos\alpha & u_{z g0} &= u_{\eta g0}\sin\alpha \end{aligned} \quad (\text{A.4})$$

The total leakage flow rate Q for spiral-grooved seals is the result of leakage flow of the land parts and the groove parts, shown here:

$$\begin{aligned} Q &= Q_l + Q_g = \pi C_{l0}[2(R+T) + C_{l0}]L_{lg}u_{z l0} \\ &\quad + I_S \left[\frac{1}{2}L_g(2C_{l0} + L_g\tan\theta)u_{g\eta 0}\sin\alpha + \frac{C_{l0}L_g}{\tan\theta}u_{\zeta 0} \right] \\ &\quad + \pi(T + C_{l0})(2R + T + C_{l0})(1 - L_{lg})u_{z g0} \end{aligned} \quad (\text{A.5})$$

Governing equations of spiral-grooved liquid seals

Figure 8 illustrates a differential element of fluid having dimensions $Rd\theta$, dz , and $H(z, \theta, t)$. The upper and lower surfaces of the element correspond to the rotor and the stator surfaces, which have velocities of $R\omega$ and zero, respectively. Under the assumptions of “fine groove theory,” the continuity and momentum equations are built and represented as follows.

Bulk-flow continuity equation:

$$\frac{\partial H}{\partial t} + \frac{\partial(Hu_\theta)}{R\partial\theta} + \frac{\partial(Hu_z)}{\partial z} = 0 \quad (\text{A.6})$$

Circumferential-momentum equation:

$$\rho H \left(\frac{\partial u_\theta}{\partial t} + u_\theta \frac{\partial u_\theta}{R\partial\theta} + u_z \frac{\partial u_\theta}{\partial z} \right) = -H \frac{\partial P}{R\partial\theta} + \tau_\theta \Big|_0^H \quad (\text{A.7})$$

Axial-momentum equation:

$$\rho H \left(\frac{\partial u_z}{\partial t} + u_\theta \frac{\partial u_z}{R\partial\theta} + u_z \frac{\partial u_z}{\partial z} \right) = -H \frac{\partial P}{\partial z} + \tau_z \Big|_0^H \quad (\text{A.8})$$

Flow within the land part was simplified as the flow between two parallel plates. The flow within the groove land is divided into the jet flow region and the vortex region. Hirs's turbulent lubrication theory is used to describe the shear stresses in the preceding equations. Hence, the fluid shear stress both in the axial direction and in the circumferential direction of the land part and the groove part can be represented as:

$$\tau_{z l} \Big|_0^H = -\rho\lambda_{z l}u_{z l}^2 \quad (\text{A.9})$$

$$\tau_{z g} \Big|_0^{H'} = -\frac{1}{2}\rho u_{z g}^2(0.25\lambda_f + \lambda_{z g}) \quad (\text{A.10})$$

$$\tau_{\theta l} \Big|_0^H = -\rho\lambda_{z l}u_{z l} \left(u_{\theta l} - \frac{1}{2}R\omega \right) \quad (\text{A.11})$$

$$\tau_{\theta g} \Big|_0^{H'} = \frac{1}{2}\rho 0.25\lambda_f u_{z g}(u_{\theta d} - u_{\theta g}) - \frac{1}{2}\rho\lambda_{z g}u_{\theta g}u_{z g} \quad (\text{A.12})$$